



**HAL**  
open science

# Three-Dimensional Magnetohydrodynamic Simulations of the Solar Wind Interaction With a Hyperfast-Rotating Uranus

L. Griton, F. Pantellini, Z. Meliani

► **To cite this version:**

L. Griton, F. Pantellini, Z. Meliani. Three-Dimensional Magnetohydrodynamic Simulations of the Solar Wind Interaction With a Hyperfast-Rotating Uranus. *Journal of Geophysical Research Space Physics*, 2018, 123 (7), pp.5394-5406. 10.1029/2018JA025331 . obspm-02296091

**HAL Id: obspm-02296091**

**<https://hal-obspm.ccsd.cnrs.fr/obspm-02296091>**

Submitted on 1 Jan 2022

**HAL** is a multi-disciplinary open access archive for the deposit and dissemination of scientific research documents, whether they are published or not. The documents may come from teaching and research institutions in France or abroad, or from public or private research centers.

L'archive ouverte pluridisciplinaire **HAL**, est destinée au dépôt et à la diffusion de documents scientifiques de niveau recherche, publiés ou non, émanant des établissements d'enseignement et de recherche français ou étrangers, des laboratoires publics ou privés.

Copyright

## RESEARCH ARTICLE

10.1029/2018JA025331

## Three-Dimensional Magnetohydrodynamic Simulations of the Solar Wind Interaction With a Hyperfast-Rotating Uranus

L. Griton<sup>1</sup> , F. Pantellini<sup>1</sup>, and Z. Meliani<sup>2</sup>
<sup>1</sup>LESIA, Observatoire de Paris, Université PSL, CNRS, Sorbonne Université, Université Paris Diderot, Sorbonne Paris Cité, Meudon, France, <sup>2</sup>LUTH, Observatoire de Paris, PSL Research University, CNRS UMR 8102, Université Paris Diderot, Meudon, France

## Key Points:

- Planetary field lines form a helical, Alfvénic structure moving downstream faster than the magnetosheath plasma
- Reconnection regions are also moving downstream and are helically shaped with a twice as large pitch
- The MHD equations have been integrated using the background/residual splitting technique for the magnetic field

## Correspondence to:

L. Griton,  
lea.griton@observatoiredeparis.psl.eu

## Citation:

Griton, L., Pantellini, F., & Meliani, Z. (2018). Three-dimensional magnetohydrodynamic simulations of the solar wind interaction with a hyperfast-rotating Uranus. *Journal of Geophysical Research: Space Physics*, 123, 5394–5406. <https://doi.org/10.1029/2018JA025331>

Received 8 FEB 2018

Accepted 5 JUN 2018

Accepted article online 13 JUN 2018

Published online 13 JUL 2018

**Abstract** We present magnetohydrodynamic simulations of a fast-rotating planetary magnetosphere reminiscent of the planet Uranus at solstice, that is, with the spin axis pointing to the Sun. We impose a 10 times faster rotation than for Uranus, in order to emphasize the effects of rotation on the magnetospheric tail without the need of an excessively large simulation domain while keeping the qualitative aspects of a supersonic magnetized solar wind interacting with a fast-rotating magnetosphere. We find that a complex helical Alfvénic structure propagates downstream at a velocity exceeding the plasma velocity in the magnetosheath. Similarly, the reconnection regions, which mediate the interaction of the planetary magnetic field and the interplanetary magnetic field, do also form a helical structure with the same downstream velocity but a 2 times larger pitch. We speculate that the magnetic field of the helical structure connected to the interplanetary magnetic field asymptotically reduces the phase velocity of the helical structure toward the tailward velocity in the magnetosheath. For our simulations we use the MPI-AMRVAC code which we enhanced with a time-dependent background magnetic field in the splitting of the magnetic field.

## 1. Introduction

Among all major planetary magnetospheres of the solar system, the magnetosphere of Uranus is the most mysterious case within reach of a spacecraft (Arridge et al., 2012). In fact, Uranus presents the largest angle between spin axis and magnetic axis of all magnetized planets of the solar system. Moreover, the large in-ecliptic-plane component of its spin axis implies important seasonal variations of the magnetospheric configuration. Like Neptune, Uranus was visited only once by the Voyager II spacecraft, during a few days around 24 January 1986. This unique flyby provided the community with enough data to establish a model for the planetary magnetic field (Connerney et al., 1987) and to measure Uranus' rotation period (Podolak & Reynolds, 1987). Subsequently, several articles devoted to the magnetosphere of Uranus were published, including studies of Uranus' magnetotail by Voight et al. (1983, 1987) and Behannon et al. (1987). These observations and first studies stimulated the realization of numerical simulations of the interaction of a low plasma  $\beta$  and a high Mach number solar wind with a fast-rotating planetary magnetosphere (17 hr rotation period) with a spin axis almost in the ecliptic plane and a large ( $\approx 60^\circ$ ) angle between the magnetic axis and the spin axis.

However, only a very limited number of simulations of the Uranian magnetosphere have been published to date. The 3-D magnetohydrodynamic (MHD) simulation by Tóth et al. (2004) provided the first illustration of the helical and time-dependent structure of the tailward stretched planetary field line. Despite not having included the interplanetary magnetic field (IMF) in their simulation, they found current sheet crossings in good agreement with the current sheet crossings from Voyager II data collected along its path through the Uranian magnetosphere. More recently, Cao and Paty (2017) used a multifluid (ions-electron) MHD code to simulate the seasonal and diurnal variations of the magnetosphere for a nonzero IMF. However, unlike Tóth et al. (2004), Cao and Paty (2017) mostly restrict their exploratory work to the near-planet region, particularly focusing on the variability of the dayside connectivity between IMF and planetary field. One of their main conclusions is that reconnection plays an important role in changing the magnetic topology of the subsolar magnetopause between open and closed over a rotation period. Despite not presenting numerical simulations one may also mention Masters (2014), who proposes an empirical model in order to determine the positions of the reconnection regions on the dayside magnetopause. In this paper we present single-fluid

MHD simulations of the Uranian magnetosphere at solstice with the major objective of investigating the effect of the IMF on the tail structure of the magnetosphere, an effect not present in Tóth et al. (2004; who use a very large simulation domain but a solar wind with no IMF) and only marginally commented on by Cao and Paty (2017). However, in order to emphasize the effect of rotation, we shorten the rotation period by a factor of 10, the major advantage of such an acceleration of the rotation being a shorter wavelength (or pitch) of the helical structure of the tail allowing for a smaller simulation domain as compared to the reference paper of Tóth et al. (2004). The scaling law connecting our fast-rotating Uranus and the real Uranus is probably not a simple one; however, there is no fundamental reason for the two cases to behave in a qualitatively very different way.

We adapted the original version of the MPI-AMRVAC code (Keppens et al., 2012) to simulate rotating planets with a strong intrinsic magnetic field plunged in a supersonic uniform flow (the solar wind). Our modified version of MPI-AMRVAC is based on the background/residual splitting technique for a time-dependent, potential, and generic axisymmetric background field  $\mathbf{B}_0$ . The details of the implemented equations are given in section 2. Simulation domain and boundary conditions are described in section 3. Normalizations and simulation parameters are presented in section 4. Finally, in section 5 we discuss simulation results corresponding to the solstice configuration of a superfast-rotating Uranus-type planet, with a spin to magnetic axis tilt angle of  $90^\circ$  (Run 1) and with the more realistic tilt angle of  $60^\circ$  (Run 2).

## 2. Simulation Model

MHD simulations have been used since the 1980s to study various astrophysical objects on a global scale. The simulation of magnetospheres of stars and planets is particularly challenging due to the presence of an intrinsic magnetic field. This intrinsic magnetic field does not change on the timescale of the relaxation time of the whole magnetosphere. It radially decreases by several orders of magnitude (and so does the Alfvén speed) on typical magnetospheric scales, whereas the variable component of the magnetic field does not vary by more than a factor of 10 or so (Tanaka, 1994). In order to circumvent the difficulty of numerically integrating the MHD equations in the presence of strong spatial gradients (without drastically reducing the spatial resolution of the numerical grid), Tanaka (1994) proposed to solve the MHD equations by splitting the global magnetic field  $\mathbf{B}$  into an intrinsic potential magnetic field  $\mathbf{B}_0$  and a residual magnetic field  $\mathbf{B}_1$ . This technique has been widely applied to MHD simulations of planetary magnetospheres since then (e.g., for recent studies of Saturn, Jia et al., 2012; Jupiter, Chané et al., 2017; or Uranus, Cao & Paty, 2017). However, in Tanaka (1994), the background magnetic field  $\mathbf{B}_0$  was assumed to be potential (i.e., current-free) and time independent. More recently, Gombosi et al. (2002) extended the splitting technique to allow for a time-dependent and nonpotential  $\mathbf{B}_0$ . This time-dependent background magnetic field is essential for the case of a fast rotator with nonaligned spin and magnetic axis such as Uranus (Tóth et al., 2004) and Neptune.

Here simulations are run using the MPI-AMRVAC code with the nonrelativistic MHD equations and a background/residual splitting technique. The total magnetic field  $\mathbf{B}$  is thus split into two components, a user-defined analytical background field  $\mathbf{B}_0$  and a residual (not necessarily small) field  $\mathbf{B}_1 = \mathbf{B} - \mathbf{B}_0$ . With this decomposition in mind we can write the resistive MHD equations (dimensionless form) for a polytropic plasma as follows:

$$\partial_t \rho + \nabla \cdot (\mathbf{v}\rho) = 0 \quad (1)$$

$$\partial_t(\rho\mathbf{v}) + \nabla \cdot (\mathbf{v}\rho\mathbf{v} - \mathbf{B}\mathbf{B} + \mathbf{B}_0\mathbf{B}_0) + \nabla(p_{\text{tot}} - \frac{1}{2}\mathbf{B}_0^2) = \mathbf{J}_0 \times \mathbf{B}_0 \quad (2)$$

$$\begin{aligned} \partial_t e_1 + \nabla \cdot [\mathbf{v}(e + p_{\text{tot}} - \mathbf{B} \cdot \mathbf{B}_0) - \mathbf{B}_1 \mathbf{B} \cdot \mathbf{v}] = & -\mathbf{B}_1 \cdot \partial_t \mathbf{B}_0 - (\mathbf{v} \times \mathbf{B}) \cdot \mathbf{J}_0 \\ & + \nabla \cdot (\mathbf{B}_1 \times \eta \mathbf{J}) + \eta \mathbf{J} \cdot \mathbf{J}_0 \end{aligned} \quad (3)$$

$$\partial_t \mathbf{B}_1 + \nabla \cdot (\mathbf{v}\mathbf{B} - \mathbf{B}\mathbf{v}) = -\partial_t \mathbf{B}_0 - \nabla \times (\eta \mathbf{J}) \quad (4)$$

where  $\rho$  is the density of mass,  $p$  the gas pressure,  $\mathbf{v}$  the flow velocity,  $e = p/(\gamma - 1) + \rho \frac{1}{2} \mathbf{v}^2 + \frac{1}{2} \mathbf{B}^2$  the total energy,  $e_1 = p/(\gamma - 1) + \rho \frac{1}{2} \mathbf{v}^2 + \frac{1}{2} \mathbf{B}_1^2$ , and  $p_{\text{tot}} = p + \frac{1}{2} \mathbf{B}^2$  the total pressure.  $\mathbf{J}_0 = \nabla \times \mathbf{B}_0$ ,  $\mathbf{J} = \mathbf{J}_0 + \mathbf{J}_1$  is the total current and  $\eta$  the magnetic diffusivity. In the nonresistive case ( $\eta = 0$ ) and for a potential and time-independent background field  $\mathbf{B}_0$ , all terms on the right of the equal sign in equations (1)–(4) vanish.

In this paper we assume a potential background field  $\mathbf{B}_0$  and zero resistivity so that nonideal effects, such as magnetic reconnection, are driven by numerical resistivity only. Accordingly, the only nonzero terms on the right-hand side of equations (2) and (3) are the terms proportional to  $\partial_t \mathbf{B}_0$ . We note that the important term  $-\partial_t \mathbf{B}_0$  in equation (4) is missing in the corresponding equation (5) of Cao and Paty (2017). This term was first presented by Gombosi et al. (2002).

Here we assume an axisymmetric planetary field  $\mathbf{B}_0$  defined through a generic a multipolar expansion  $\mathbf{B}_0 = \sum_{l=1}^n (B_{0,r}^l \mathbf{e}_r + B_{0,\theta}^l \mathbf{e}_\theta + B_{0,\varphi}^l \mathbf{e}_\varphi)$  in spherical coordinates with

$$B_{0,r}^l(r, \cos \theta) = (l + 1) \frac{\psi_l}{r} \quad (5)$$

$$B_{0,\theta}^l(r, \cos \theta) = \frac{\psi_l A_l}{r} \quad (6)$$

$$B_{0,\varphi}^l(r, \cos \theta) = 0 \quad (7)$$

where

$$\psi_l(r, \cos \theta) = \left(\frac{1}{r}\right)^{l+1} g_l P_l(\cos \theta), \quad (8)$$

and

$$A_l(\cos \theta) = \left(\frac{P_{l-1}(\cos \theta)}{\cos \theta P_l(\cos \theta)} - 1\right) \frac{l \cos \theta}{(1 - \cos^2 \theta)^{1/2}}, A_l(0) = 1. \quad (9)$$

In the above expressions,  $P_l$  are the  $l$ th Legendre polynomials,  $\theta$  the polar angle with respect to the magnetic axis, and  $r$  the distance to the center of the planet (expansion center). The background field is thus assumed to be axisymmetric (no dependence on the azimuthal angle  $\varphi$ ).

Let us further discuss the case of a time-varying  $\mathbf{B}_0$ , and let us specialize to the case of  $\mathbf{B}_0$  rotating about a spin axis  $\boldsymbol{\omega}$  ( $\omega = |\boldsymbol{\omega}|$  being the angular velocity of rotation) crossing the magnetic field expansion center  $r = 0$ . In that case the term  $\partial_t \mathbf{B}_0$  appearing in equation (4) can be written as

$$\partial_t \mathbf{B}_0 = \nabla \times (\mathbf{v}_{\text{cor}} \times \mathbf{B}_0) = \boldsymbol{\omega} \times \mathbf{B}_0 - \mathbf{v}_{\text{cor}} \cdot \nabla \mathbf{B}_0, \quad (10)$$

where  $\mathbf{v}_{\text{cor}} \equiv \boldsymbol{\omega} \times \mathbf{r}$  is the corotation velocity. The first term on the right-hand side of (10) is easily computed for arbitrary orientations of the spin vector  $\boldsymbol{\omega}$ . The second term on the right-hand side of (10) implies the explicit computation of the spatial derivatives of  $\mathbf{B}_0$  which we give hereafter

$$\partial_r B_{0,r}^l(r, \cos \theta) = -(l + 1)(l + 2)g_l P_l r^{-(l+3)} \quad (11)$$

$$\partial_\theta B_{0,r}^l(r, \cos \theta) = -B_r^l A_l \quad (12)$$

$$\partial_r B_{0,\theta}^l(r, \cos \theta) = -(l + 1 + r) \frac{\psi_l A_l}{r} \quad (13)$$

$$\partial_\theta B_{0,\theta}^l(r, \cos \theta) = -(A_l^2 - \partial_\theta A_l) \frac{\psi_l}{r} \quad (14)$$

$$\partial_\theta A_l(\cos \theta) = \frac{l(l + 1)(P_l^2 - P_{l-1}P_{l+1})}{(1 - \cos^2 \theta)P_l^2}. \quad (15)$$

We note that the time derivative of  $B_0$  can also be computed numerically as in Tóth et al. (2004). Since, in the general case, the magnetic axis moves with respect to the simulation frame, a time-dependent transformation matrix which transforms the components from the magnetic frame into the simulation frame needs to be implemented to complete the program.

**Table 1**  
Planetary and Solar Wind Parameters Used in the Simulations

Run	IMF	$B_{SW}$ (nT)	Tilt angle	$g_1$ (nT)	$\beta_{SW}$	$M_{SW}$	$\omega$	$v_{SW}$ (km/s)
1	+y	0.2	90°	95.14	0.1	20	6.42	400
2	+y	0.2	60°	95.14	0.1	20	6.42	400

Note. The tilt angle is the angle between the spin axis and the magnetic axis. The rotation axis points toward  $-z$ .  $\beta_{SW}$  is the wind thermal to magnetic pressure ratio and  $M_{SW}$  the wind sonic Mach number.  $\omega$  is in normalized units and corresponds to 10 times the angular velocity of Uranus. Rotation period is  $t_{rot} = 2\pi/\omega = 0.98t_0$ . IMF = interplanetary magnetic field.

### 3. Simulation Domain and Boundary Conditions

We simulate a hyperfast-rotating Uranus, as a spherical magnetized body rotating in a stationary magnetized supersonic solar wind. The reference frame of the simulation is a right-handed Cartesian frame with the  $z$  axis pointing against the solar wind flow. The spin axis is aligned with the  $z$  axis (in reference to the solstice configuration of Uranus). The  $x$  axis is such that the planetary dipole vector is confined to the  $(x, z)$  plane at  $t = 0$ , with positive  $x$  and  $z$  components. The  $y$  axis completes the right-handed coordinate system. We denote as *magnetic axis* the symmetry axis of the planet's magnetic field. The simulation domain is delimited by two concentric spherical shells. The spherical grid spans from  $r = 1$  (inner boundary) to  $r = 40.1$  (outer boundary) with a number of grid points (72, 24, 48) in  $r$ ,  $\theta$ , and  $\varphi$ , respectively, for a total number of 82,944 simulation cells. At the inner boundary, we impose a free outflow condition for the radial velocity  $\partial_r v_r = 0$  and corotation velocity  $\omega \times \mathbf{r}$  for the tangential components. Density and pressure are arbitrarily set to solar wind density and  $\gamma = 5/3$  times the solar wind plasma pressure, respectively. Neumann conditions are applied to  $\mathbf{B}_1$ . At the outer boundary, solar wind conditions are imposed, unless the density in any cell close to the boundary departs by more than 1% from the theoretical value in which case a Neumann boundary condition  $\partial_r = 0$  is applied to all fields (free outflow condition).

We do not need to explicitly specify a resistive layer to mimic an ionosphere at the inner boundary as the numerical resistivity due to the finite grid resolution is sufficiently strong not to have to assign a nonzero resistivity in the MHD equations. For the given spatial resolution, the relative strength of the resistive electrical field  $\vec{E}_{res} = (\vec{v}_{corot} - \vec{v}) \times \vec{B}$  with respect to the (ideal) peak corotation electric field at the surface  $\vec{v}_{corot} \times \vec{B}_{eq}$  observed in our simulations is generally of the order or less than 10% except around the magnetic poles where it can reach 40%.

### 4. Normalizations and Simulation Parameters

Distances are normalized to the inner boundary radius  $R_0$ , with  $R_0 = 5R_U$  ( $R_U$  is the radius of Uranus). Velocities are normalized to the sound speed in the solar wind  $c_{SW} = (\gamma p_{SW} / \rho_{SW})^{1/2}$  and the time to  $t_0 = R_0 / c_{SW}$ . We neglect the shift of  $0.3R_U$  of Uranus' dipole. It should be noted, however, that the smallest cell size in the system is of the order 2–3 times the planet radius  $R_U$ , so we do not expect the effect of a  $0.3R_U$  displacement to be significant. Planetary field is given as a planetary-centered dipole. Uranus has effectively a significant quadrupole term near the surface, but since it decreases faster than the dipole term it becomes negligible at  $5R_U$ . In order to keep computational time and the domain extent within reasonable limits, we reduce the Uranus rotation period by a factor of 10.

The simulation parameters are summarized in Table 1. We choose typical  $\beta$ , Mach number, and solar wind magnetic field at a distance of 20 AU (Burlaga et al., 1998; Richardson & Smith, 2003). The solar wind velocity ( $v_{SW} = 400$  km/s) is typical of a slow wind. The dipole coefficient  $g_1$  corresponds to the value of  $g_1^0$  given for Uranus by Connerney et al. (1987), at a distance of  $R_0 = 5R_U$ .

### 5. Results and Discussion

We discuss the results of two simulations with identical wind parameters and rotation axis but different orientations of the planetary magnetic field axis (see Table 1). Run 1 concerns a fast-rotating Uranus whose tilt angle is 90°, such that both magnetic poles play a symmetric part over a rotation. Run 2 is closer to the real configuration of Uranus, with a tilt angle of 60°, so that one of the magnetic poles is always facing the incoming solar wind, while the other one is always on the nightside.

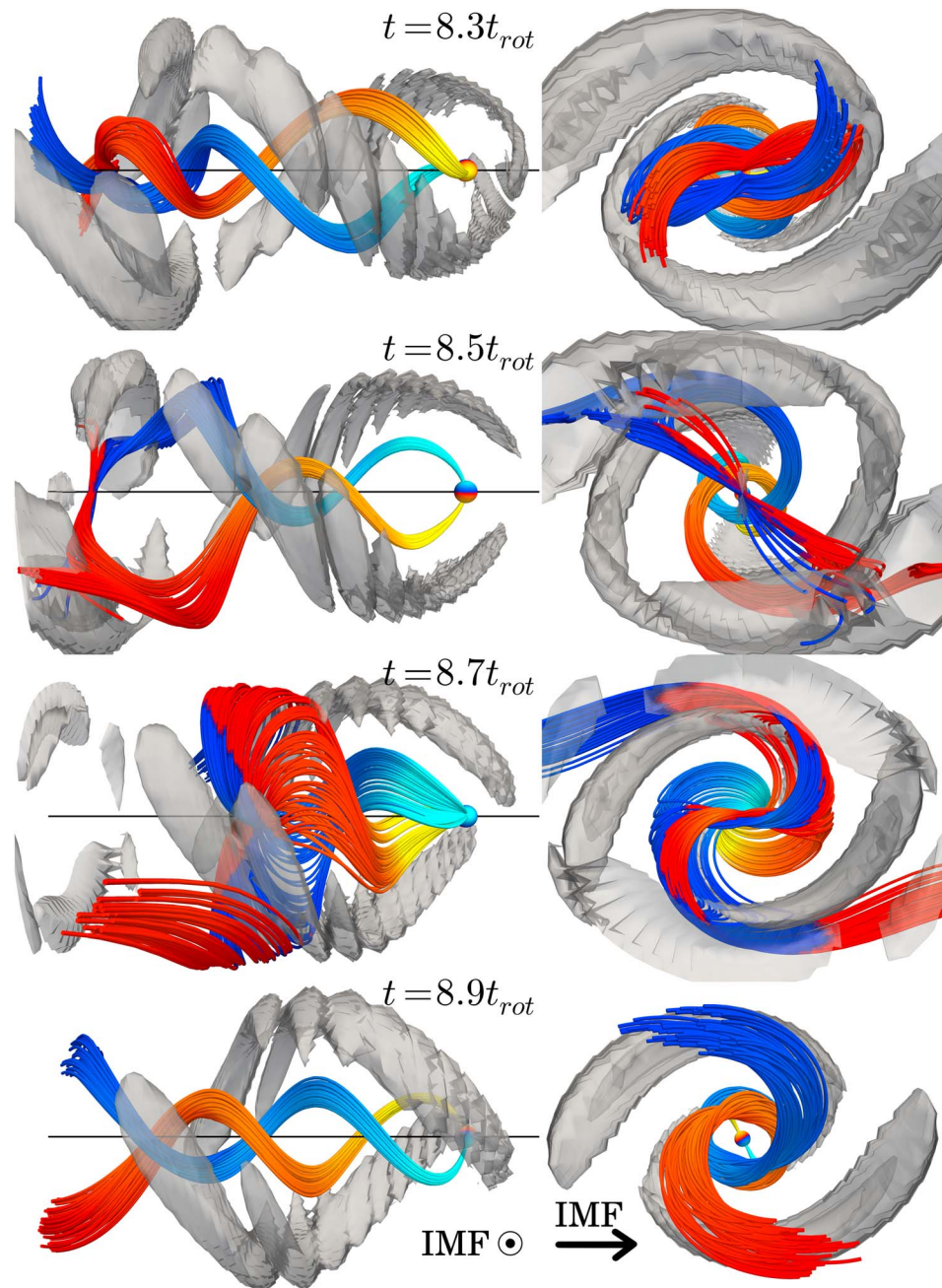


**Figure 1.** Run 1: side view (left column) and associated view from the tail (right column) of a sample of magnetic field lines connected to the magnetic positive pole (yellow-to-red lines) and to the magnetic negative pole (cyan-to-blue lines). Gray contours delimit volumes where  $\beta \geq 20$ , a condition we use as a proxy to identify reconnection sites. The dark line is the rotation axis (z axis). The x axis points upward in all plots.

### 5.1. The 90° Tilt Angle Case

Planet rotation generates a double-helical structure of planet connected magnetic field lines and reconnection sites (Figure 1). Reconnection sites are characterized by high  $\beta$  values. We use the high  $\beta$  instead of the high current density because the latter does not discriminate between reconnection sites and the shock. High  $\beta$ , as mentioned in Cao and Paty (2017), is an interesting parameter for reconnection because it shows the area of both high temperatures and very low magnetic field intensity, both being characteristic of reconnection sites. As shown in Figure 1, the spatial structure of north and south connected lines are out of phase by a half wavelength, as expected due to the symmetry of the whole system (system is invariant with respect to

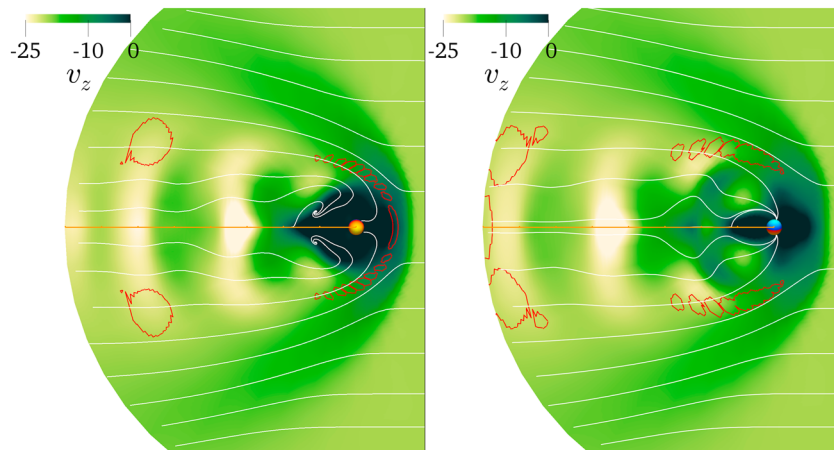


**Figure 2.** Run 1: Contours of  $v_z$  and velocity streamlines in the  $y = 0$  plane ( $x$  axis points upward) at  $t = 8.3t_{\text{rot}}$  (left) and a quarter of rotation later (right). The orange line represents a distance of 40, from the center of the simulation domain to the outer boundary, along the planetary spin axis. The red contours show the location of the reconnection sites ( $\beta \geq 15$ ).

reflections at the  $x = 0$  and  $y = 0$  planes). The pitch of the helical structure of the reconnection sites is roughly twice the pitch of the magnetic field lines ( $\approx 12.5R_0$ ; see Figure 2). The two structures move downstream at the same phase velocity so that at a fixed position downstream of the planet, the temporal periodicity of the reconnection sites is twice the temporal periodicity of the magnetic field. At  $t = 8.3t_{\text{rot}}$  (Figure 1, first row) the planetary magnetic axis is approximately parallel to the IMF orientation and is therefore favorable for reconnection at the subsolar point (Figure 2, left). During the other phases of the rotation, the reconnection sites are localized off axis only. Reconnection sites are places where the IMF and planetary field become connected or disconnected. Planetary field lines extending downstream close to the  $z$  axis and far from the reconnection sites (as for the lines in Figure 1 at  $t = 8.3t_{\text{rot}}$  or  $t = 8.9t_{\text{rot}}$ ) present a neat helical structure with a regular pitch. Planetary lines that approach the reconnection sites (particularly visible at  $t = 8.7t_{\text{rot}}$ ) make large excursions in the direction perpendicular to  $z$  with an essentially vanishing pitch; that is, field components perpendicular to  $z$  are dominant.

The  $z = -15R_0$  cut of Figure 3 shows that the downstream directed fluid velocity  $v_z$  (all velocities are normalized to the sound speed in the solar wind; see section 4) is largest ( $\approx -25$ ) for these IMF connected field lines. Since these field lines are perpendicular to the fluid velocity vector (and the velocity field is incompressible), they must travel at the fluid velocity by virtue of the frozen-in theorem.  $v_z = -25$  is effectively the asymptotic velocity of the whole structure in the downstream region. Figure 3 also shows that planet connected field lines of the type shown in Figure 1 at  $t = 8.7t_{\text{rot}}$  (i.e., not connected with the IMF at or upstream of  $z = -15R_0$ ) are embedded in a much slower plasma flowing at  $v_z \approx -15$ . These lines thus support an Alfvénic fluctuation propagating downstream in the plasma frame at a phase velocity of the order of  $-10$  ( $-200$  km/s in SI units) to keep in phase with the global motion of the whole helical structure.

In general, the helical structure moves downstream faster than the fluid velocity in both the magnetosheath and the solar wind. The question is as follows: what determines the overall velocity of the structure (and thus the helical pitch)? Some authors suggest that because of the Alfvénic nature of the structure, it should travel at the Alfvén speed. In the Tóth et al. (2004) simulations where there is no IMF field and no direct connection between the helical structure formed by the planetary field lines and the solar wind, the propagation speed of the whole structure (in the plasma frame) should be of the order of the Alfvén speed, especially when the field lines are elongated in the  $z$  direction as for their much more slowly rotating planet. The discrepancy between propagation speed and Alfvén speed in the Tóth et al. (2004) simulations is attributed by the authors to frictional forces through the magnetopause. In our simulation we do effectively observe that the helical structure is formed by propagating Alfvén waves, leaving no doubts about the Alfvénic nature of the structure. However, we argue that the IMF connected planetary field lines play an essential role in regulating the downstream motion of the helical magnetic structure. To verify this intuition, we run our simulations twice, once with the IMF, and once with the IMF set to 0 nT. We observe that in the case without IMF, the wavelength of the helical structure is constant. However, in the case with IMF, the wavelength of the helical structure has a length

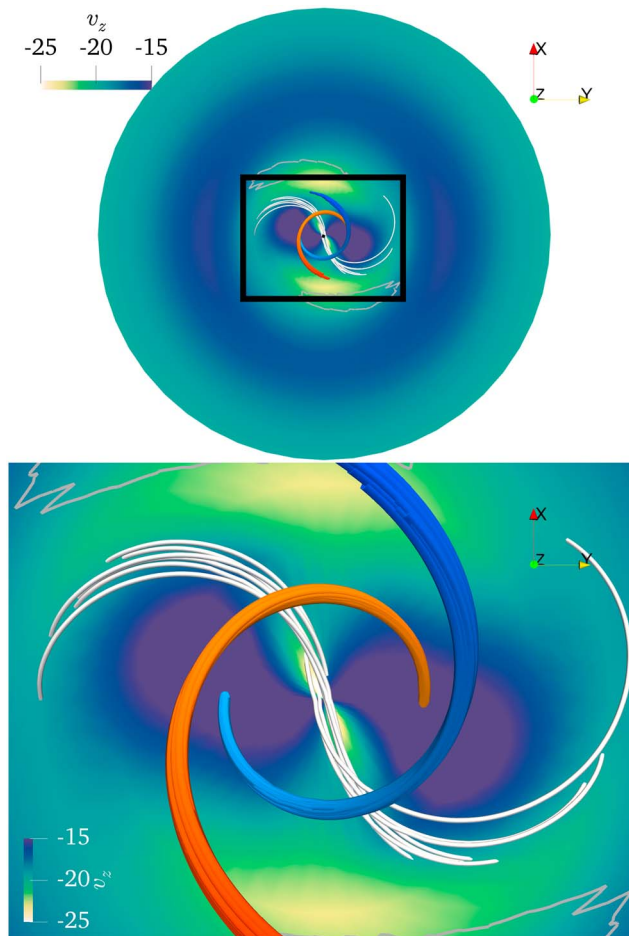


**Figure 3.** Run 1: contours of  $v_z$  in the  $z = -15R_0$  plane (seen from the tail), at  $t = 8.7t_{\text{rot}}$  (top), along with a zoom of the black squared area (bottom). The color scheme shows areas flowing tailward slower (blue), faster (yellow to white) than the solar wind (traveling at  $v_z = -20$ ). Red and blue stream tracers show a sample of magnetic field lines connected to the planet and twisted in a double helix as in Figure 1. These nearly  $z$ -aligned field lines are embedded in two distinct slowly flowing plasma regions. Each of these two regions is populated with field lines connected to one particular magnetic hemisphere of the planet. The white stream tracers show magnetic field lines crossing the rotation axis. They are embedded in a fast-flowing plasma and have a small  $B_z$  thus separating the slow field regions with different  $B_z$  polarity. Such lines are either planetary lines connected to the IMF through the magnetopause at the planet's location or pure planetary lines with each foot connected to a different magnetic hemisphere of the planet. They may also be pure IMF lines. In any case these lines do not extend significantly downstream of the plane under consideration. IMF = interplanetary magnetic field.

87% of the length of the corresponding wavelength in the no-IMF simulation, showing that the propagation of the helix is slowed down by the IMF.

The global structure of the magnetic field lines and of the flow pattern is different from usual schemes proposed for fast rotators in more *Earth-like* configurations, as Saturn or Jupiter (see chapters 5, 6, and 12 from Keiling et al., 2015, and references therein). From our simulation we do extract the following scenario:

1. IMF field lines that connect to the planetary magnetic field, when upstream or immediately downstream of the planet, become retarded by the rotation (such field lines are not visible in Figure 1) with the portion of field lines in the magnetosheath in advance with respect to the portion inside the magnetopause.
2. During the retardation phase, the portion of the field lines inside the magnetopause becomes accelerated to high tailward velocities by the torque due to the Lorentz force. The lines going through the fast flow regions of Figure 3 are representative of such accelerated lines which travel faster than their *foot* in the magnetosheath thus reducing the overall distortion of the retarded field lines. These lines thus slide along the surface of the magnetopause at a velocity that is globally larger than the fluid velocity in the



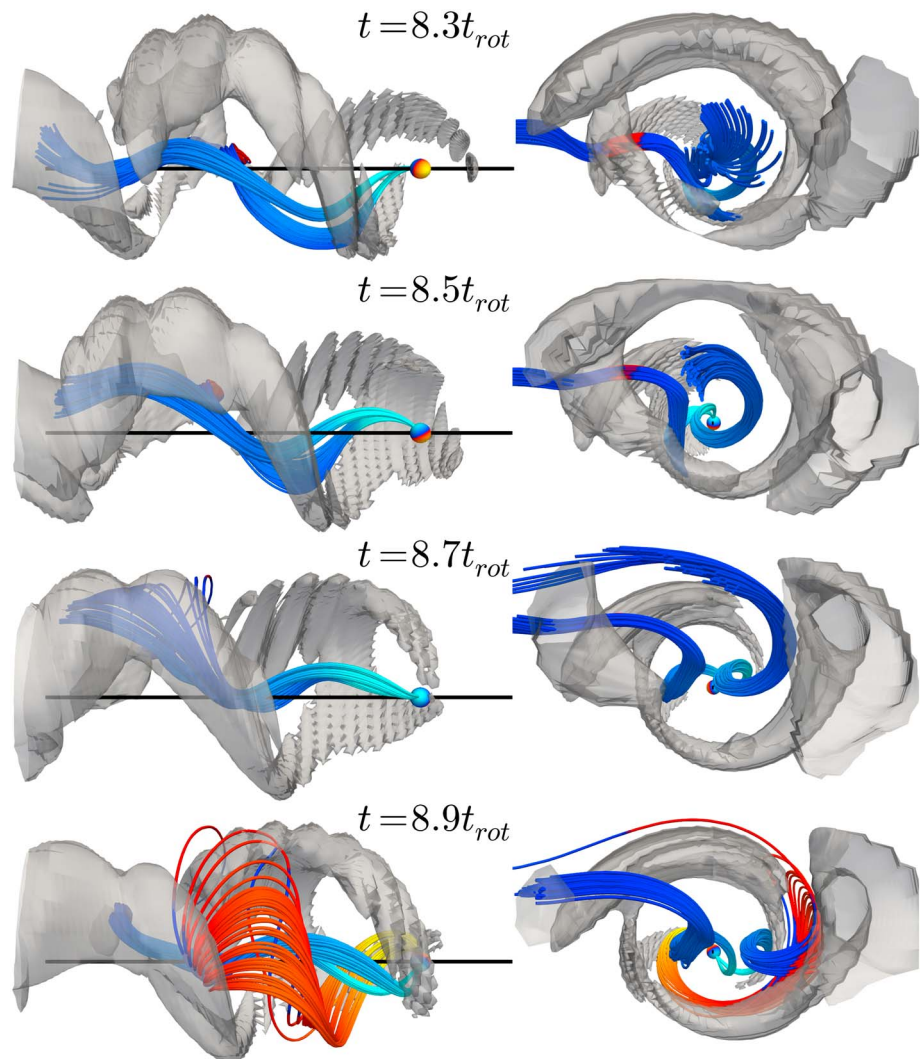


**Figure 4.** Run 2: side view (left column) and associated view from the tail (right column) of a sample of magnetic field lines connected to the positive magnetic pole (yellow-to-red lines) and to the negative magnetic pole (cyan-to-blue lines). Gray contours delimit volumes where  $\beta \geq 20$ , a proxy for reconnection. The dark line indicates the rotation axis (z axis). The x axis points upward in all plots.

magnetosheath. Eventually, a portion of the field lines encounters a reconnection region (volumes delimited by gray surfaces in Figure 1) where it disconnects completely from the planet, transforming into a slowly moving magnetosheath line.

3. Other magnetosheath lines, downstream of a reconnection region, may also connect to the planet as the reconnection regions move faster than the plasma in the magnetosheath. We argue that as a consequence of these exchanges between IMF field and planetary field the helical structure is asymptotically slowed down to the magnetosheath plasma velocity (which tends toward the solar wind velocity at large distances down the tail). This is based on our comparison between our simulations with and without IMF. However, in our simulation with IMF, the downstream extension of the simulation domain is too small to allow for a measurable deceleration of the helical structure. For example, no significant deceleration of the high-velocity spots in Figure 2 could be observed.
4. In the simulation, the observed tailward velocity of the helical structure is roughly 50% higher than the flow velocity in the magnetosheath. We argue that this difference is a function of the time during which a planetary magnetic field line stays connected to the IMF. In other words, it depends on the interval of time during which the tailward velocity of a portion of the line (transverse to the z axis) is significantly slower

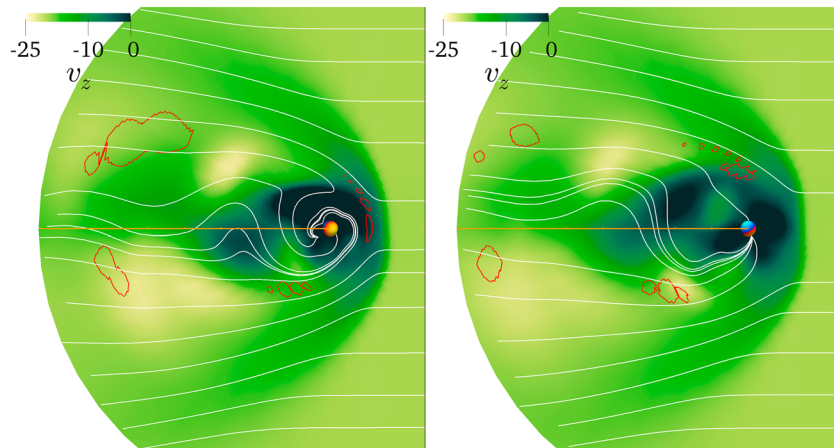


**Figure 5.** Run 2: contours of  $v_z$  and velocity stream lines in the  $y = 0$  plane ( $x$  axis points upward) at  $t = 8.3t_{\text{rot}}$  and a quarter of rotation later. The orange line represents a distance of 40, from the center of the simulation domain to the outer boundary, along the planetary spin axis. The red contours show the location of the reconnection sites ( $\beta \geq 15$ ).

than its counterpart in the magnetosheath, that is, essentially during the time that the portion of the line in the low-velocity region (the dark regions in Figure 2) has a significant transverse component.

It may be noted that despite the somewhat different spin and magnetic axis orientations, the reconnection sites in the simulation are similarly shaped and show a similar temporal variations as in the Masters' (2014) empirical model (second line in his Figure 5). Here and in Masters' paper reconnection sites largely cover the dayside magnetopause (along a direction parallel to the  $x$  axis) at time  $t = 8.3t_{\text{rot}}$  when the IMF and the planetary magnetic axis are nearly parallel (case h in Figure 5 of Masters, 2014). No dayside reconnection sites are visible half a period later, whereas small, roughly diagonally opposed reconnection spots appear at intermediate orientations.

In Figure 2, the bow shock is visible on the velocity contours, and one may notice that its shape and intensity vary over a rotation period (if one compares the figure on the left and the one on the right, a quarter of rotation later), especially in the dayside. This is a consequence of the change in the reconnection sites location, particularly of the subsolar once-per-rotation favorable reconnection site. Figure 2 also illustrates the downstream motion of the reconnection sites (red contours) and the fluid velocity fluctuations in the  $y = 0$  plane. In the  $y = 0$  plane, the flow pattern, reconnection sites, and the shape of the bow shock are symmetric by construction with respect to the  $z$  axis. A symmetry which obviously no longer exists in the  $60^\circ$  tilt case will be discussed in the next section.

### 5.2. The $60^\circ$ Tilt Angle Case

In Run 2, the helical structure of the connected magnetic field lines is not as clear as in Run 1 (see Figure 4). This is a logical consequence of the fact that over a full rotation period one of the planetary poles is always on the nightside and the other on the dayside, thus breaking the symmetry between the two poles of Run 1. The downstream phase velocity of the structure is the same as in Run 1 ( $v = -25$ ), so that planetary axis orientation does not seem to affect significantly the average pitch of the helical structure once it has been accelerated. However, downstream fluid velocities peak at slightly lower levels (as one may notice by comparing Figures 2 and 5) which is essentially a consequence of the fact that in Run 2 there are no magnetic field lines oriented perpendicularly to the  $z$  axis in the central region close to the  $z$  axis so that fluid and phase velocity do not have to be equal.

Another major difference is the off- $z$  axis displacement of tail structures (evident in all Figures 5–7). As shown in Figure 6, the regions with the fastest plasma are now only located off  $z$  axis, with no fast streams crossing the close to  $z$  axis region of slow plasma. The  $z = -15R_0$  slice of Figure 7 shows that there are two regions of fast plasma regions rotating at different and nonconstant angular velocities so that they sometimes appear to merge (e.g., near  $t = 8.9t_{\text{rot}}$ ). The two regions are magnetically connected to each of the two magnetic poles of the planet and sometimes to both as at  $t = 8.5t_{\text{rot}}$ . In general, the region connected to the nightside pole is spatially well delimited and can be tracked during most of the cycle while the dayside connected region is often spread out over a large angular interval.

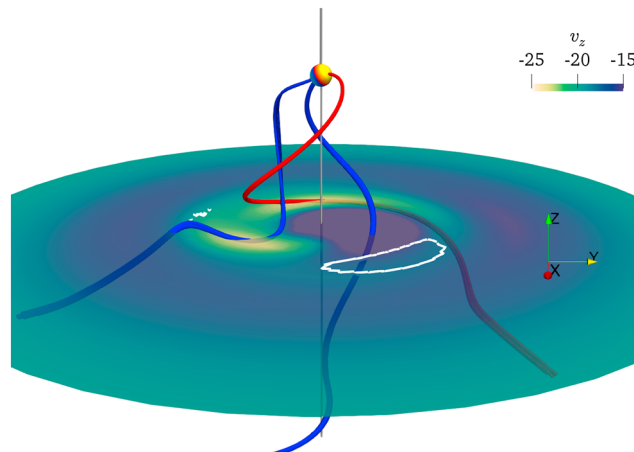


**Figure 6.** Run 2: slice of the simulation domain at  $z = -15R_0$  and  $t = 8.16t_{\text{rot}}$ . The three magnetic field lines are connected to the positive planetary magnetic pole (red stream tracer) and to the negative planetary magnetic pole (blue stream tracers), respectively. White contours correspond to  $\beta = 15$  and thus delimit reconnection sites. The gray vertical line is the rotation axis ( $z$  axis). Note that the field lines cross the plane in regions with large and slow fluid velocities depending on whether their transverse component is dominant or not.

At large distances down the tail, beyond the acceleration region, one may use the sign of  $B_z$  in order to identify the magnetic hemisphere to which the magnetic field lines inside the magnetopause are connected to. Figure 8 confirms that at  $z = -15R_0$  the magnetic field lines closest to the  $z$  axis are all connected to the night-side hemisphere of the planet. The dayside connected lines are always located immediately underneath the magnetopause so that during some phases of the cycle, as for example at  $t = 8.5t_{\text{rot}}$ , the central region (with all lines connected to the nightside planetary hemisphere) is completely surrounded by a region with lines having an opposite  $B_z$  polarity, some of which (the ones inside the magnetopause) are connected to the day-side magnetic hemisphere of the planet. Phases where the innermost region is at least in part surrounded by a region of opposite  $B_z$  polarity can be observed in Figure 13 of Tóth et al. (2004) even though their Figure 17

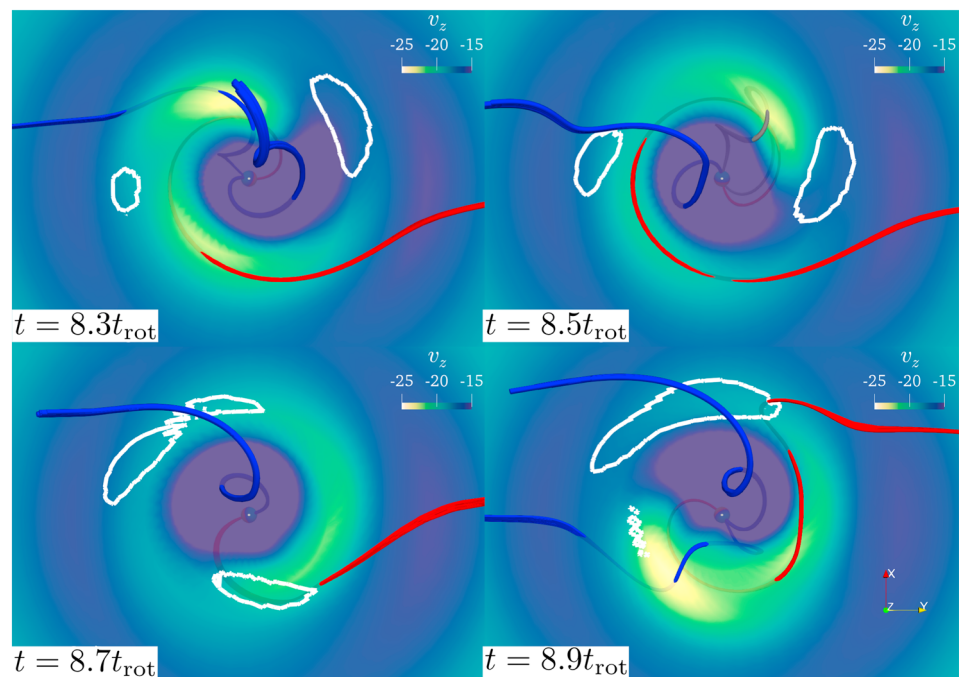


**Figure 7.** Run 2: slice of the simulation domain at  $z = -15R_0$  (seen from the tail with  $x$  axis pointing upward), at four different times. The magnetic field lines are connected to the positive planetary magnetic pole (red line) or to the negative planetary magnetic pole (blue lines) or to both poles (gray lines).

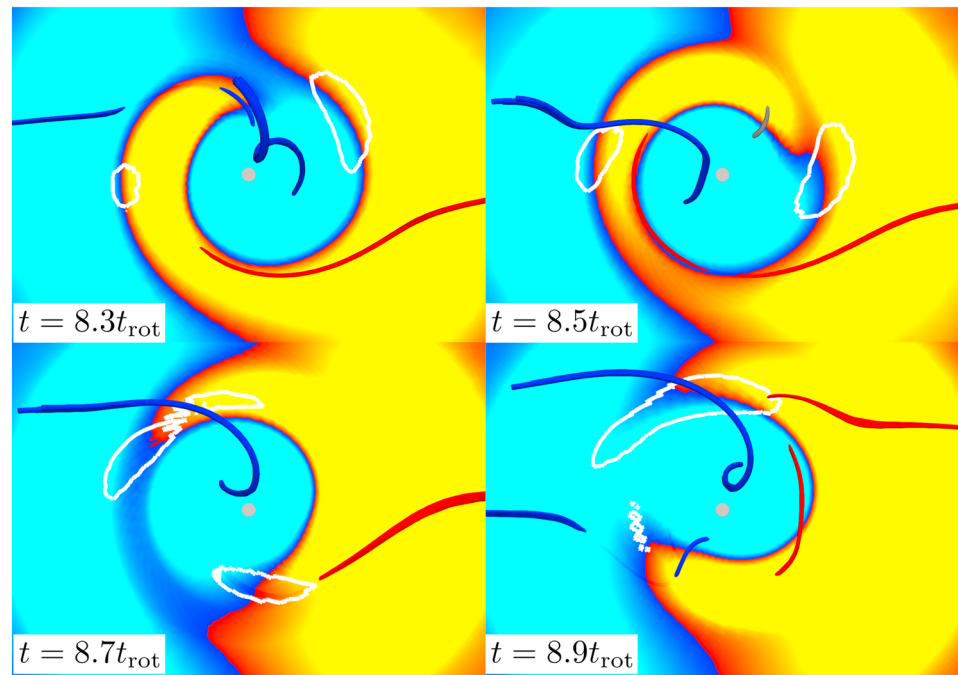


**Figure 8.** Run 2: slice of the simulation domain at  $z = -15R_0$  (seen from the tail with  $x$  axis pointing upward); yellow-red contours indicate areas where  $B_z < 0$ , while cyan-blue contours indicate  $B_z \geq 0$ , at four different times. Red and blue magnetic field lines are either connected to the positive or the negative planetary magnetic pole. Gray field lines are connected to both poles (closed field lines). White contours correspond to  $\beta = 15$  (delimiting reconnection regions). The large gray dot shows the rotation axis ( $z$  axis).

does not show a close to  $z$  axis region dominated by one single  $B_z$  polarity. However, the central part of each of the four panels of Figure 8 can be compared with Figures 3a–3c from Schulz and McNab (1996).

## 6. Conclusion

We have presented MHD simulations of the interaction of the solar wind with the magnetosphere of a hyperfast-rotating Uranus for solstice orientation of the planetary spin axis, that is, spin axis pointing to the Sun. The solar wind is a low-beta, high-Mach number and magnetized plasma with a magnetic field oriented perpendicular to the flow velocity. The reason for shortening Uranus rotation period by a factor of 10, thus reducing the difference between the rotation period and the Alfvénic crossing time, was double: first, a substantial reduction of both computational time and computational domain size with the implied advantage of limiting numerical diffusion in time; and second, an enhancement of the effects of the rotation on the structure of the magnetospheric tail, as, for example an improved visibility of the reconnection regions due to the shortening of the tailward fluctuations of the magnetic field. Obviously, our results cannot be directly transposed to the real Uranus as no simple scaling law may exist.

The first of the two simulations of a hyperfast Uranus is for an unrealistic spin to planetary magnetic axis orientation of  $90^\circ$ . The run has the advantage of presenting a reduced complexity, with the two planetary magnetic poles playing a symmetric role. As a consequence of the symmetry of the whole system, the field lines from each of the two planetary poles describe two interpenetrating helices stretching downstream of the planet (Figure 1). The tailward velocity of the helical structure ( $\approx 25$ ) is substantially larger than the plasma velocity in the solar wind ( $\approx 20$ ) and in the magnetosheath ( $\approx 17$ ; Figures 2 and 3). In our simulation the tailward velocity of the helical structure is reached within a rather short distance downstream of the planet. That distance is of the order of the distance covered by an IMF field line in the magnetosheath during one rotation period, which leads us to speculate that the velocity of the helical structure is driven by the IMF field lines retarded during the time they are connected to the planet. The fluid velocity in fixed planes transverse to the rotation axis is also highly variable in space and time with mostly slow plasma ( $< 15$ ) near the axis and high velocities ( $> 20$ ) below and at the magnetopause. The helical structure is thus a complex, highly nonlinear,

Alfvén wave embedded in a flowing plasma. We speculate that at large downstream distances (beyond the boundary of the simulation domain) the velocity of the structure will be asymptotically slowed down to the level of the fluid velocity in the magnetosheath. We do not observe such a deceleration in our simulation, the downstream region being probably too short, but we argue that the deceleration is inevitable because of the field lines in the helical structure connected to the IMF. The most visible illustration of the interaction of the helical structure with the IMF are the reconnection regions which in the simulation are observed to reach the downstream domain boundary. In the 90° run the reconnection regions also show a double-helical structure with a pitch 2 times the pitch of the magnetic structure.

In the second simulation of a hyperfast Uranus we choose spin to planetary magnetic axis of 60°, roughly the angle of the real planet. Under such circumstances, the two planetary magnetic poles no longer play a symmetric role, one pole being always located on the dayside and the other on the nightside of the planet. The main consequence is that the nice downstream helical structure of both the magnetic field lines and the reconnection region is now broken (Figure 4). In particular, while in the 90° case the two reconnection arms are always positioned at 180° relative to each other in any plane perpendicular to the spin axis, in the 60° case the relative position of the two arms is highly variable. Interestingly, the downstream-directed phase speed of the whole structure in the 60° simulation is the same as in the 90° simulation, probably because the magnetic axis orientation is still mainly transverse to both the wind velocity direction and the spin axis. Thus, the average helical pitch turns out to be identical in the two simulations. However, in the 60° run, the pitch tends to be shorter/longer than average depending on the phase (Figures 5–7). As for the symmetric run, no significant deceleration of the helical structure could be observed.

Finally, from the more technical point of view, we have used the background/residual splitting technique of the magnetic field for a time-varying background field for the first time in MPI-AMRVAC. We have selected the planetary intrinsic magnetic field  $B_0$  as the background field which is a time-varying field in the (inertial) frame of the simulation. For completeness, the analytic expressions of  $\partial_t B_0$  for the case of an arbitrary oriented multipolar and axisymmetric magnetic field have been extensively presented in section 2.

#### Acknowledgments

No new observational data were used for this work. Simulation results can be obtained by contacting the first author. The Plas@par project is acknowledged for financial support. The work of Léa Griton was supported by the CNES (Centre national d'Etudes spatiales) and the Observatoire de Paris (contract reference 5100016058). Some computational tests made use of the High Performance Computing OCCIGEN and JADE at CINES within the DARI project c2015046842. The authors thank Michel Moncuquet for his helpful comments.

#### References

- Arridge, C. S., Agnor, C. B., André, N., Baines, K. H., Fletcher, L. N., Gautier, D., et al. (2012). Uranus Pathfinder: Exploring the origins and evolution of Ice Giant planets. *Experimental Astronomy*, 33, 753–791.
- Behannon, K. W., Lepping, R. P., Sittler Jr., E. C., Ness, N. F., Mauk, B. H., Krimigis, S. M., & McNutt, R. L. (1987). The magnetotail of Uranus. *Journal of Geophysical Research*, 92, 15,354–15,366.
- Burlaga, L. F., Ness, N. F., Wang, Y.-M., & Sheeley, N. R. (1998). Heliospheric magnetic field strength out to 66 AU: Voyager 1, 1978–1996. *Journal of Geophysical Research*, 103(A10), 23,727–23,732. <https://doi.org/10.1029/98JA01433>
- Cao, X., & Paty, C. (2017). Diurnal and seasonal variability of Uranus's magnetosphere. *Journal of Geophysical Research: Space Physics*, 122, 6318–6331. <https://doi.org/10.1002/2017JA024063>
- Chané, E., Saur, J., Keppens, R., & Poedts, S. (2017). How is the Jovian main auroral emission affected by the solar wind?. *Journal of Geophysical Research: Space Physics*, 122, 1960–1978. <https://doi.org/10.1002/2016JA023318>
- Connerney, J. E. P., Acuña, M. H., & Ness, N. F. (1987). The magnetic field of Uranus. *Journal of Geophysical Research*, 92(A13), 15,329–15,336. <https://doi.org/10.1029/JA092iA13p15329>
- Gombosi, T. I., Tóth, G., Zeeuw, D. L. D., Hansen, K. C., Kabin, K., & Powell, K. G. (2002). Semirelativistic magnetohydrodynamics and physics-based convergence acceleration. *Journal of Computational Physics*, 177(1), 176–205. <http://www.sciencedirect.com/science/article/pii/S0021999102970099>
- Jia, X., Hansen, K. C., Gombosi, T. I., Kiverson, M. G., Tóth, G., DeZeeuw, D. L., & Ridley, A. J. (2012). Magnetospheric configuration and dynamics of Saturn's magnetosphere: A global MHD simulation. *Journal of Geophysical Research*, 117, A05225. <https://doi.org/10.1029/2012JA017575>
- Keiling, A., Jackman, C. M., & Delamere, P. A. (Eds.) (2015). *Magnetotails in the solar system*, Geophysical Monograph Series (Vol. 207). Washington, DC: American Geophysical Union.
- Keppens, R., Meliani, Z., van Marle, A. J., Delmont, P., Vlasis, A., & van der Holst, B. (2012). Parallel, grid-adaptive approaches for relativistic hydro and magnetohydrodynamics. *Journal of Computational Physics*, 231(3), 718–744. <http://www.sciencedirect.com/science/article/pii/S0021999111000386>, Special Issue: Computational Plasma Physics.
- Masters, A. (2014). Magnetic reconnection at Uranus' magnetopause. *Journal of Geophysical Research: Space Physics*, 119, 5520–5538. <https://doi.org/10.1002/2014JA020077>
- Podolak, M., & Reynolds, R. T. (1987). The rotation rate of Uranus, its internal structure, and the process of planetary accretion. *Icarus*, 70, 31–36.
- Richardson, J. D., & Smith, C. W. (2003). The radial temperature profile of the solar wind. *Geophysical Research Letters*, 30, 1206. <https://doi.org/10.1029/2002GL016551>
- Schulz, M., & McNab, M. C. (1996). Source-surface modeling of planetary magnetospheres. *Journal of Geophysical Research*, 101, 5095–5118.
- Tanaka, T. (1994). Finite volume TVD scheme on an unstructured grid system for three-dimensional MHD simulation of inhomogeneous systems including strong background potential fields. *Journal of Computational Physics*, 111(2), 381–389. <http://www.sciencedirect.com/science/article/pii/S0021999184710710>
- Tóth, G., Kovács, D., Hansen, K. C., & Gombosi, T. I. (2004). Three-dimensional MHD simulations of the magnetosphere of Uranus. *Journal of Geophysical Research*, 109, A11210. <https://doi.org/10.1029/2004JA010406>

- Voight, G.-H., Behannon, K. W., & Ness, N. F. (1987). Magnetic field and current structures in the magnetosphere of Uranus. *Journal of Geophysical Research*, 92, 15,337–15,346.
- Voight, G.-H., Hill, T. W., & Dessler, A. J. (1983). The magnetosphere of Uranus—Plasma sources, convection, and field configuration. *The Astrophysical Journal (ApJ)*, 266, 390–401.